

Article

CO Oxidation over Metal Oxide (La₂O₃, Fe₂O₃, PrO₂, Sm₂O₃, and MnO₂) Doped CuO-Based Catalysts Supported on Mesoporous Ce_{0.8}Zr_{0.2}O₂ with Intensified Low-Temperature Activity

Yan Cui ^{1,†}, Leilei Xu ^{1,†,*}, Mindong Chen ^{1,*}, Chufei Lv ¹, Xinbo Lian ¹, Cai-e Wu ², Bo Yang ¹, Zhichao Miao ³, Fagen Wang ⁴ and Xun Hu ^{5,*} 

¹ Collaborative Innovation Center of the Atmospheric Environment and Equipment Technology, School of Environmental Science and Engineering, Nanjing University of Information Science & Technology, Jiangsu Key Laboratory of Atmospheric Environment Monitoring and Pollution Control, Nanjing 210044, China

² College of Light Industry and Food Engineering, Nanjing Forestry University, Nanjing 210037, China

³ School of Chemistry and Chemical Engineering, Shandong University of Technology, Zibo 255049, China

⁴ School of Chemistry and Chemical Engineering, Jiangsu University, 301 Xuefu Road, Zhenjiang 212013, China

⁵ School of Material Science and Engineering, University of Jinan, Jinan 250022, China

* Correspondence: leileixu88@gmail.com (L.X.); chenmdnuist@163.com (M.C.); Xun.Hu@outlook.com (X.H.)

† These authors equally contributed to this work.

Received: 7 August 2019; Accepted: 26 August 2019; Published: 28 August 2019



Abstract: CuO-based catalysts are usually used for CO oxidation owing to their low cost and excellent catalytic activities. In this study, a series of metal oxide (La₂O₃, Fe₂O₃, PrO₂, Sm₂O₃, and MnO₂)-doped CuO-based catalysts with mesoporous Ce_{0.8}Zr_{0.2}O₂ support were simply prepared by the incipient impregnation method and used directly as catalysts for CO catalytic oxidation. These mesoporous catalysts were systematically characterized by X-ray powder diffraction (XRD), N₂ physisorption, transmission electron microscopy (TEM), energy-dispersed spectroscopy (EDS) mapping, X-ray photoelectron spectroscopy (XPS), and H₂ temperature programmed reduction (H₂-TPR). It was found that the CuO and the dopants were highly dispersed among the mesoporous framework via the incipient impregnation method, and the strong metal framework interaction had been formed. The effects of the types of the dopants and the loading amounts of the dopants on the low-temperature catalytic performances were carefully studied. It was concluded that doped transition metal oxides could regulate the oxygen mobility and reduction ability of catalysts, further improving the catalytic activity. It was also found that the high dispersion of rare earth metal oxides (PrO₂, Sm₂O₃) was able to prevent the thermal sintering and aggregation of CuO-based catalysts during the process of calcination. In addition, their presence also evidently improved the reducibility and significantly reduced the particle size of the CuO active sites for CO oxidation. The results demonstrated that the 15CuO-3Fe₂O₃/M-Ce₈₀Zr₂₀ catalyst with 3 wt. % of Fe₂O₃ showed the best low-temperature catalytic activity toward CO oxidation. Overall, the present Fe₂O₃-doped CuO-based catalysts with mesoporous nanocrystalline Ce_{0.8}Zr_{0.2}O₂ solid solution as support were considered a promising series of catalysts for low-temperature CO oxidation.

Keywords: CuO-based catalyst; Fe₂O₃ dopant; mesoporous Ce_{0.8}Zr_{0.2}O₂ solid solution; low-temperature catalytic activity; CO oxidation

1. Introduction

CO emitted from industrial processes and automobile exhaust has been one of the most serious environmental issues for a long time, and is greatly harmful to human health and the living environment [1,2]. To control and reduce the emission of carbon monoxide, its catalytic oxidation has been widely considered to be the most efficient solution from the standpoint of environmental considerations. To date, the research related to catalyst systems for the CO oxidation process have mainly been focused on the noble metal- and transition metal oxide-based supported catalysts. Precious metal-based catalysts (such as Pt, Au, etc.) have attracted extensive research interest due to their outstanding low-temperature catalytic activity [3–5]. For example, the Au-based catalyst in the CO oxidation process is able to completely convert CO into CO₂ at $-70\text{ }^{\circ}\text{C}$ [6]. As a comparison, traditional metal oxide-based catalysts usually require relatively higher temperatures to obtain superior activity. Although noble metal (such as Pt, Au)-based catalysts usually show high activity for the CO catalytic oxidation reaction at low reaction temperatures, their wide application has been restricted by their high cost and limited availability. Therefore, supported catalysts based on transitional metal oxides with high catalytic activity (such as CuO, Co₃O₄, etc.) have attracted increasing attention due to their excellent catalytic activity and economical properties [7–9].

Co₃O₄-based catalysts have been widely studied for their exceptional low-temperature catalytic activities, which are comparable to those of noble metal-based catalysts [9,10]. However, the Co₃O₄-based catalysts usually suffer quick deactivation under high humidity. As a comparison, CuO-based catalysts have a strong tolerance to the moisture, although its low-temperature activity is relatively poor [11]. Therefore, the development and fabrication of CuO-based catalysts with excellent low-temperature activity toward CO oxidation is commonly considered a research hotspot and an ongoing challenge in this field.

It is widely believed that the activity of CuO-based catalysts is greatly affected by the types and the preparation strategies of the catalysts. Among the CuO-based catalysts, CuO-CeO₂-based metal oxide catalysts have become the most promising candidates for CO oxidation process due to their outstanding redox performance and low cost [12], and because their catalytic performance is excellent, being comparable even to the noble metal-based catalysts [13]. The reason for their high catalytic activity might be that the Cu species is highly active, and exhibits exceptional co-chemical adsorption by Cu²⁺-Cu⁺ couple with CeO₂ support. Meanwhile, CeO₂ support has the capacity for storage and release of oxygen due to the presence of oxygen vacancy, which could promote the activation of the oxygen. Specifically, it has oxidation-coupled Ce⁴⁺/Ce³⁺, which could activate oxygen molecules during CO oxidation [14]. However, pure CeO₂ usually exhibits poor thermal stability. Therefore, the incorporation of transition or rare earth metal oxides (such as ZrO₂, PrO_x, etc.) into the lattice of the CeO₂ structure can significantly improve the thermal stability of CeO₂ during high-temperature calcination [15,16]. For instance, although the incorporated ZrO₂ does not participate in the catalytic reaction, it can modify the structure and the site of CeO₂ lattice by forming Ce-Zr solid solution. This greatly improves the oxygen storage capacity (OSC), thermal stability, and the dispersion of mixed oxides [17,18]. Additionally, previous research has suggested that the synergistic effect between CuO and Ce-Zr solid solutions could enhance the catalytic oxidation activity toward CO [19].

Compared with traditional metal oxide catalytic supports, mesoporous metal oxides usually provide higher specific surface areas, bigger pore volumes, and more uniform pore channels [20]. Therefore, they can be used as efficient catalytic supports or catalysts. If the mesoporous Ce-Zr solid solution can be used as the support of CuO-based catalyst, a high dispersion of CuO over the catalysts can be obtained due to the advantageous structural properties of the supports [21]. Therefore, it has great potential to further improve low-temperature catalytic performance toward CO oxidation by providing sufficient accessible active sites for gaseous reactants.

In recent years, great efforts have been devoted to improving the low-temperature catalytic activity of CuO-based catalysts, especially by doping various catalytic promoters, including transition metal oxides (such as MnO₂, Fe₂O₃, etc.) [22–24] and rare earth metal oxides (such as Sm₂O₃, PrO₂, La₂O₃, etc.) [25–28]. Among them, the incorporation of transition metal oxides into CuO-based catalysts

can adjust the oxygen mobility and reducing ability of catalyst, which could further improve the catalytic activity. It has also been found that the presence of rare earth metal oxides could achieve high dispersion of the CuO active sites. As a result, the agglomeration of CuO-based catalysts could effectively be prevented. Furthermore, the reductivity and particle size of the CuO could be promoted, which is beneficial to the formation of the active sites for CO oxidation [29].

Herein, $\text{Ce}_{0.8}\text{Zr}_{0.2}\text{O}_2$ solid solution with a mesoporous nanocrystalline structure was successfully synthesized by evaporation-induced self-assembly (EISA) [30]. A series of CuO-based catalysts doped with different transition metal oxides and rare earth metal oxides was prepared with mesoporous $\text{Ce}_{0.8}\text{Zr}_{0.2}\text{O}_2$ solid solution support. Various characterizations, such as XRD, N_2 physisorption, TEM, EDS-mapping, XPS, and H_2 -TPR, were used to systematically characterize both the supports and catalysts. The effects of the types of different metal oxides dopants and their loading amounts on low-temperature catalytic activities toward CO oxidation were thoroughly studied.

2. Results and Discussion

2.1. Characterizations of the Support and Catalysts

2.1.1. XRD Analysis

To investigate the crystalline phase states of the support and catalysts, the XRD analyses were carried out. Figure 1(1) displayed the XRD patterns of the M-Ce80Zr20 support and 15CuO-3MO_x/M-Ce80Zr20 (MO_x = La₂O₃, Fe₂O₃, PrO₂, Sm₂O₃, MnO₂) catalysts, respectively. It is worth noting that both the support and catalysts exhibited four pronounced diffraction peaks around $2\theta = 28.6^\circ$, 33.04° , 47.4° and 56.36° , suggesting the presence of the cubic crystalline structure similar to the cubic CeO₂ (PDF#34-0394). Furthermore, the absence of ZrO₂ diffraction peaks indicates that the ZrO₂ had been successfully incorporated into the CeO₂ lattice to form a solid solution while maintaining the fluorite crystalline structure [31]. It was found that the intensities of the CuO diffraction peaks (PDF#45-0937) over 15CuO-3MO_x/M-Ce80Zr20 catalysts were highly similar with each other due to the identical CuO loading (15 wt. %). However, pristine 15CuO/M-Ce80Zr20 catalyst without any modification displayed a slightly stronger CuO diffraction peak intensity than that of the modified catalysts, which could be attributed to the poor dispersion of CuO species over M-Ce80Zr20 support due to the thermal agglomeration. This also implied that the incorporation of the MO_x metallic oxide was helpful for improving the dispersion of CuO species over the surface of the catalysts.

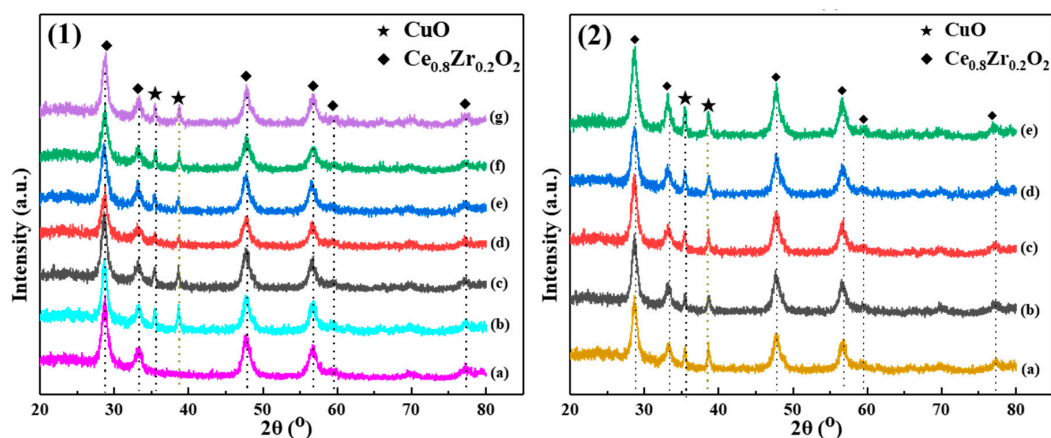


Figure 1. (1) XRD patterns of M-Ce80Zr20 and 15CuO-3MO_x/M-Ce80Zr20 (MO_x = La₂O₃, Fe₂O₃, PrO₂, Sm₂O₃, MnO₂): (a) M-Ce80Zr20, (b) 15CuO/M-Ce80Zr20, (c) 15CuO-3Fe₂O₃/M-Ce80Zr20, (d) 15CuO-3Sm₂O₃/M-Ce80Zr20, (e) 15CuO-3PrO₂/M-Ce80Zr20, (f) 15CuO-3La₂O₃/M-Ce80Zr20, (g) 15CuO-3MnO₂/M-Ce80Zr20. (2) XRD patterns of 15CuO-zFe₂O₃/M-Ce80Zr20: (a) 15CuO/M-Ce80Zr20, (b) 15CuO-1Fe₂O₃/M-Ce80Zr20, (c) 15CuO-3Fe₂O₃/M-Ce80Zr20, (d) 15CuO-5Fe₂O₃/M-Ce80Zr20, (e) 15CuO-7Fe₂O₃/M-Ce80Zr20.

The XRD patterns of 15CuO-zFe₂O₃/M-Ce80Zr20 catalysts with different CuO loading amounts are exhibited in Figure 1(2). It can be observed that the CuO diffraction peaks are very similar in intensity when the Fe₂O₃ loading amount is less than 5 wt. %. However, the intensity of the CuO diffraction peak undergoes an intense increase when the Fe₂O₃ content is further increased from 5 wt. % to 7 wt. %. This indicates that the dispersion of CuO species over the catalyst surface gradually becomes worse with increasing amounts of Fe₂O₃ loading. As a result, the growth of the crystalline size of the CuO nanoparticles would take place, which might be attributable to the limited surface area of the M-Ce80Zr20 support.

2.1.2. N₂ Physisorption Analysis

N₂ physisorption analyses were conducted to investigate the textural properties of the M-Ce80Zr20 support and the catalysts. The N₂ adsorption–desorption isotherms (panel A) and pore size distributions (panel B) of the M-Ce80Zr20 support, as well as the investigated catalysts in this study, are shown in Figure 2. As displayed in Figure 2A(1 and 2), almost all of the 15CuO-3MO_x/M-Ce80Zr20 (MO_x = La₂O₃, Fe₂O₃, PrO₂, Sm₂O₃, MnO₂) and 15CuO-zFe₂O₃/M-Ce80Zr20 catalysts exhibited type IV isotherms with H2-shaped hysteresis loops, which were highly similar to the isotherm of M-Ce80Zr20 support and 15CuO/M-Ce80Zr20 pristine catalyst. This indicates that the mesoporous structure of the catalysts had been successfully retained after doping the metallic oxide. The corresponding pore size distribution curves of these mesoporous catalysts are shown in Figure 2B(1 and 2). It can be observed that the pore size distribution curves of these catalysts display narrow pore size distribution curves centered in the range of 9.6–17.5 nm. Furthermore, it is worth noting that the catalysts display slightly larger pore diameters than those of M-Ce80Zr20, suggesting that the thermal shrinkage of the mesoporous frameworks or channels did not take place, and that the M-Ce80Zr20 support demonstrates excellent thermal stability. Furthermore, the size of the pore diameter further confirms that the pore diameters of these catalysts are located in the mesopore range (2.0–50.0 nm) [32].

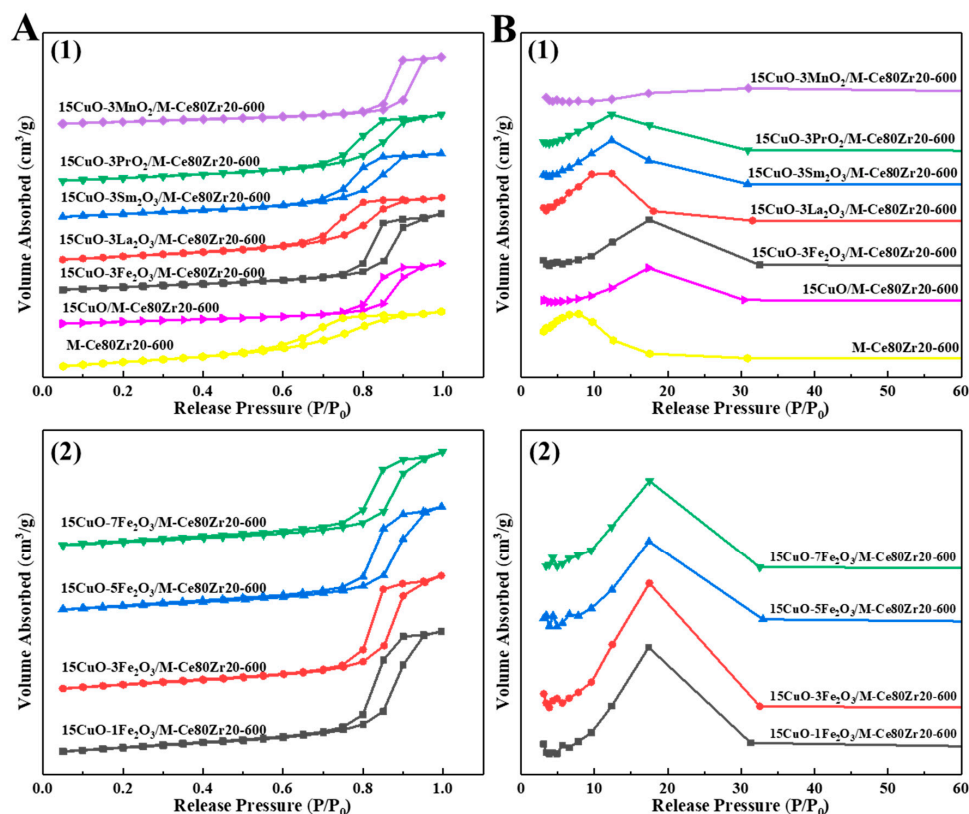


Figure 2. N₂ adsorption-desorption isotherms (A) and pore size distributions (B) of the catalytic support and the catalysts: (1) M-Ce80Zr20 and 15CuO-3MO_x/M-Ce80Zr20 (MO_x = La₂O₃, Fe₂O₃, PrO₂, Sm₂O₃, MnO₂), (2) 15CuO-zFe₂O₃/M-Ce80Zr20.

The specific structural properties of the M-Ce80Zr20 support and catalysts are summarized in Table 1. It can be found that the introduction of metal oxides generally led to the decrease of specific surface areas and the increase of mesopore diameters. For the specific surface areas and pore volumes, the 15CuO-3MO_x/M-Ce80Zr20 and 15CuO-zFe₂O₃/M-Ce80Zr20 catalysts doped with metal oxides displayed relatively smaller values due to the slight blockage of the mesopore. Additionally, the 15CuO/M-Ce80Zr20, 15CuO-3MO_x/Ce80Zr20, and 15CuO-zFe₂O₃/M-Ce80Zr80 catalysts exhibited slightly bigger average pore diameters than the M-Ce80Zr20 support. Specifically, the pore diameter of the catalysts doped with La₂O₃, PrO₂, MnO₂, and Sm₂O₃ were about 12.7 nm, and the pore diameters of the samples doped with Fe₂O₃ with various loading amounts were about 17.5 nm, which is slightly higher than those of the M-Ce80Zr20 support (7.9 nm) and the 15CuO/M-Ce80Zr20 catalyst (9.6 nm).

Table 1. Textual properties of M-Ce80Zr20 catalytic support and catalysts.

Samples	Specific Surface Area (m ² /g)	Pore Volume (cm ³ /g)	Average Pore Diameter (nm)	Isotherm Type
M-Ce80Zr20	68.9	0.12	7.9	IV H2
15CuO/M-Ce80Zr20	55.2	0.13	9.6	IV H2
15CuO-3Mn ₂ O ₃ /M-Ce80Zr20	31.1	0.13	13.0	IV H2
15CuO-3PrO ₂ /M-Ce80Zr20	48.4	0.14	12.3	IV H2
15CuO-3Sm ₂ O ₃ /M-Ce80Zr20	48.9	0.14	12.3	IV H2
15CuO-3La ₂ O ₃ /M-Ce80Zr20	54.8	0.14	12.4	IV H2
15CuO-3Fe ₂ O ₃ /M-Ce80Zr20	43.8	0.16	17.5	IV H2
15CuO-1Fe ₂ O ₃ /M-Ce80Zr20	44.5	0.17	17.4	IV H2
15CuO-5Fe ₂ O ₃ /M-Ce80Zr20	39.5	0.14	17.4	IV H2
15CuO-7Fe ₂ O ₃ /M-Ce80Zr20	37.3	0.13	17.5	IV H2

2.1.3. TEM, SAED, STEM, and EDS-Mapping Analyses

Figure 3 shows the TEM and SAED images of the M-Ce80Zr20, 15CuO/M-Ce80Zr20 and 15CuO-3MO_x/M-Ce80Zr20 (MO_x = La₂O₃, Fe₂O₃, PrO₂, Sm₂O₃, MnO₂) catalysts. For the M-Ce80Zr20 support, the mesoporous structure with a worm-like porous network formed by the stacking of Ce-Zr solid solution nanoparticles around the P123 template can be clearly observed in Figure 3a. Based on its HRTEM image in Figure 3b, it can be observed that the lattice fringe spacing of the M-Ce80Zr20 support is in the range of 0.299–0.309 nm, which may correspond to the (1 1 1) crystal plane of mesoporous Ce_{0.8}Zr_{0.2}O₂ solid solution. From SAED (inset of Figure 3a), the clear diffraction rings could be observed, indicating high crystallinity of mesoporous walls. This is well consistent with the conclusion based on the above XRD analysis in Figure 1.

The TEM images of the 15CuO-3MO_x/M-Ce80Zr20 catalysts in Figure 3c,e,g,i,k,m exhibit the same mesoporous structure as their corresponding M-Ce80Zr20 support with worm-like porous structure. However, no obvious large CuO cluster is observed, even when the CuO loading amount is as high as 15 wt. %, indicating that CuO nanoparticles are well dispersed on the surface of mesoporous M-Ce80Zr20 support. However, compared with the mesoporous Ce-Zr solid solution support, the HRTEM images of the catalysts exposed to the new crystal faces with different lattice stripe spacings about 0.230 nm and 0.250 nm, which could be attributed to the (1 1 1) and (0 0 2) crystal faces of CuO, respectively. Additionally, clear SAED diffraction rings can be observed in Figure 3c,e,g,i,k,m, indicating that these CuO-based mesoporous catalysts possess good crystalline properties.

Scanning transmission electron microscope (STEM) and EDS-mapping were carried out to investigate the spatial distribution of the elements among the mesoporous structure of the catalysts. The STEM and EDS-mapping images of 15CuO-3MO_x/M-Ce80Zr20 (MO_x = La₂O₃, Fe₂O₃, PrO₂, Sm₂O₃, MnO₂) catalysts are shown in Figure 4. It can be seen that Ce, Cu, Zr, and corresponding doped metal elements were uniformly distributed among the catalysts, suggesting that the high dispersion of the Cu and metal dopants over the surface of M-Ce80Zr20 had been achieved by the incipient impregnation method.

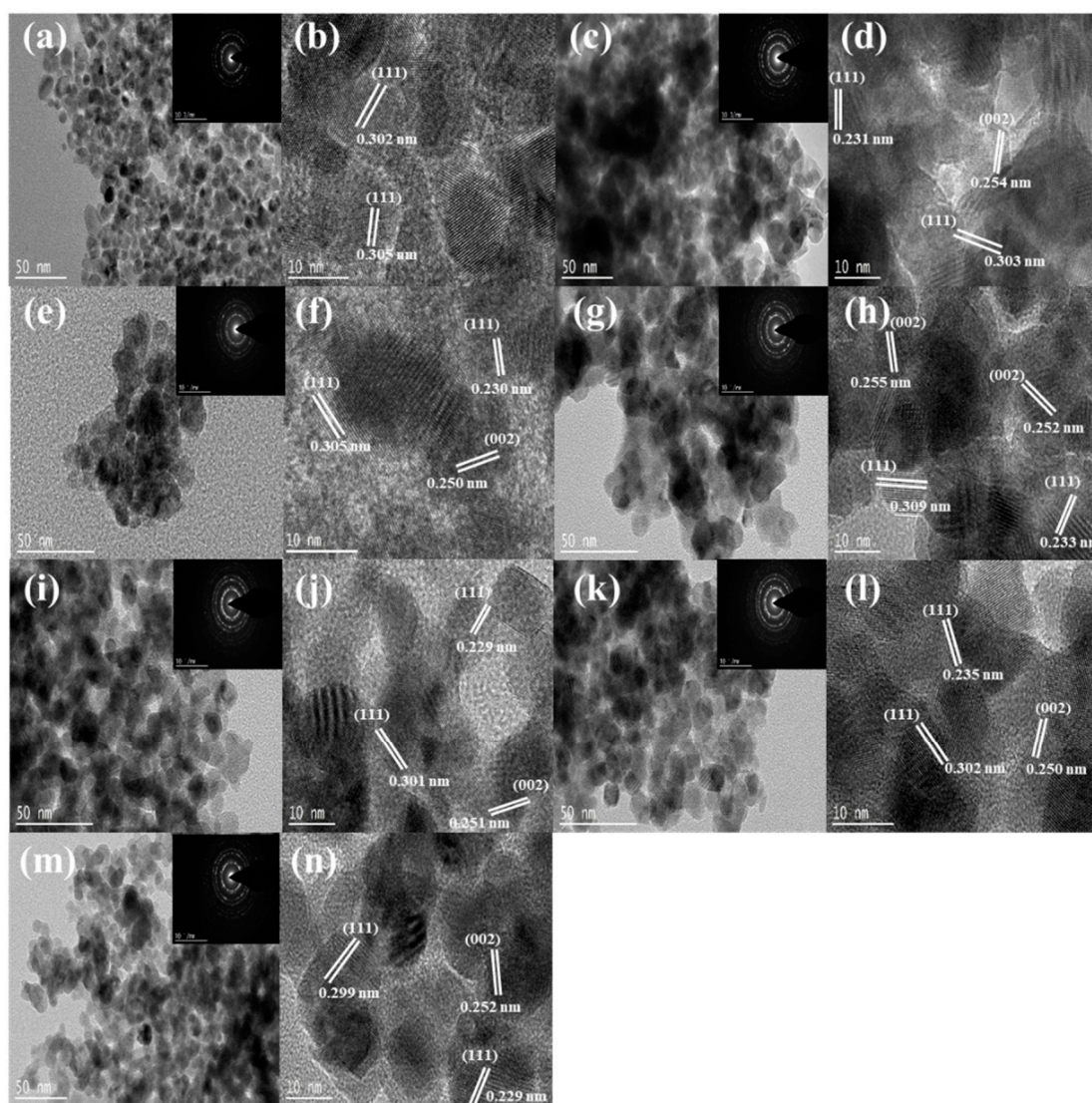


Figure 3. TEM and SAED inset of the M-Ce80Zr20 support and 15CuO-3MO_x/M-Ce80Zr20 (MO_x = La₂O₃, Fe₂O₃, PrO₂, Sm₂O₃, MnO₂) catalysts: (a,b) M-Ce80Zr20, (c,d) 15CuO/M-Ce80Zr20, (e,f) 15CuO-3Fe₂O₃/M-Ce80Zr20, (g,h) 15CuO-3MnO₂/M-Ce80Zr20, (i,j) 15CuO-3La₂O₃/M-Ce80Zr20, (k,l) 15CuO-3Sm₂O₃/M-Ce80Zr20, (m,n) 15CuO-3PrO₂/M-Ce80Zr20.

The TEM and SAED analyses of the mesoporous catalysts with different Fe₂O₃ loading amounts were carried out and their images are displayed in Figure 5. It can also be seen from Figure 5 that the (1 1 1) crystal plane of mesoporous Ce-Zr solid solution, as well as the (1 1 1) and (0 0 2) crystal planes of CuO, can be clearly observed on catalysts with various Fe₂O₃ contents. However, the crystal plane of the iron oxides (FeO_x) was absent, regardless of its loading amount. This indicates that the Fe species were highly dispersed over the surface of the catalysts, which had been proved by the EDS-mapping analysis. Additionally, the SAED diagram in the insets of Figure 5 showed clear diffraction rings, indicating that their mesoporous framework structure was in the form of a good crystalline structure.

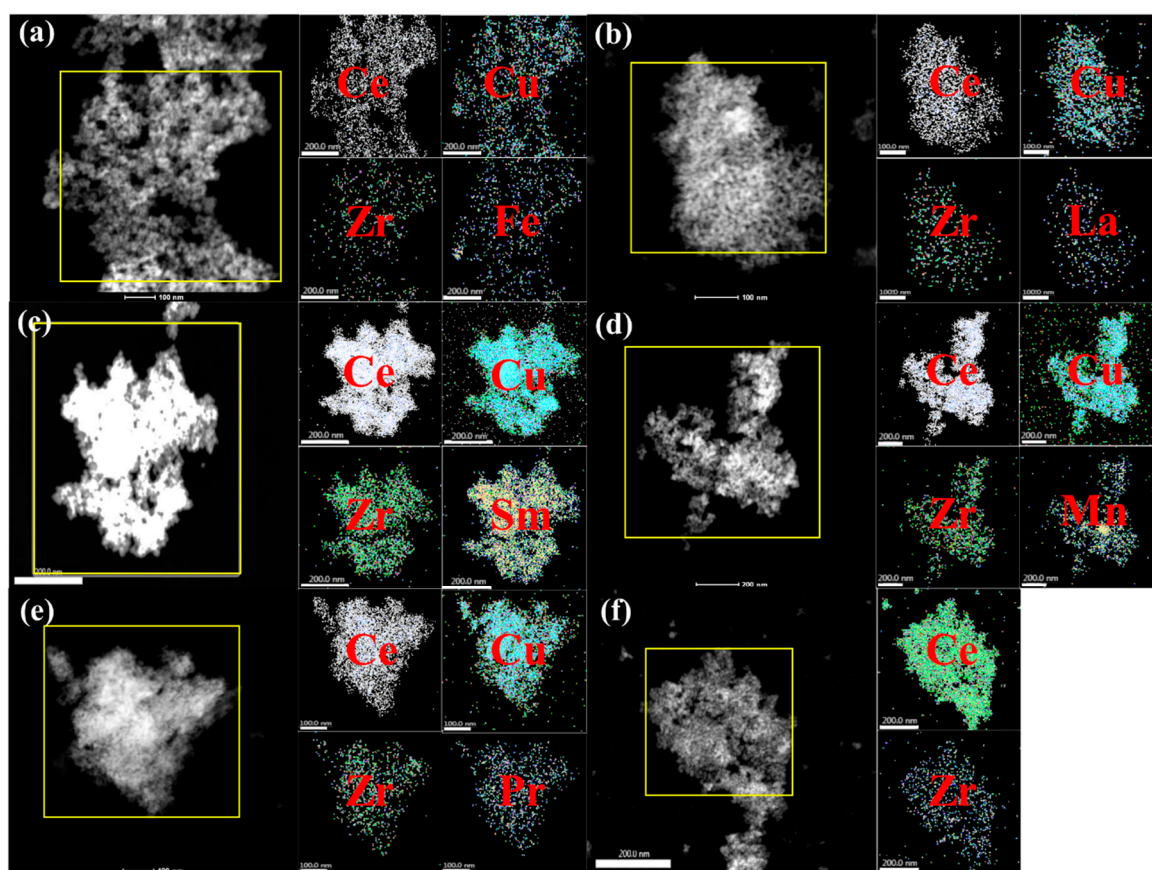


Figure 4. STEM and EDS element mapping images showing the spatial distribution of Ce, Zr, Cu and M (M = Fe, La, Sm, Mn, Pr) elements: (a) $15\text{CuO}-3\text{Fe}_2\text{O}_3/\text{M}-\text{Ce}_{80}\text{Zr}_{20}$, (b) $15\text{CuO}-3\text{La}_2\text{O}_3/\text{M}-\text{Ce}_{80}\text{Zr}_{20}$, (c) $15\text{CuO}-3\text{Sm}_2\text{O}_3/\text{M}-\text{Ce}_{80}\text{Zr}_{20}$, (d) $15\text{CuO}-3\text{MnO}_2/\text{M}-\text{Ce}_{80}\text{Zr}_{20}$, (e) $15\text{CuO}-3\text{PrO}_2/\text{M}-\text{Ce}_{80}\text{Zr}_{20}$, (f) $\text{M}-\text{Ce}_{80}\text{Zr}_{20}$.

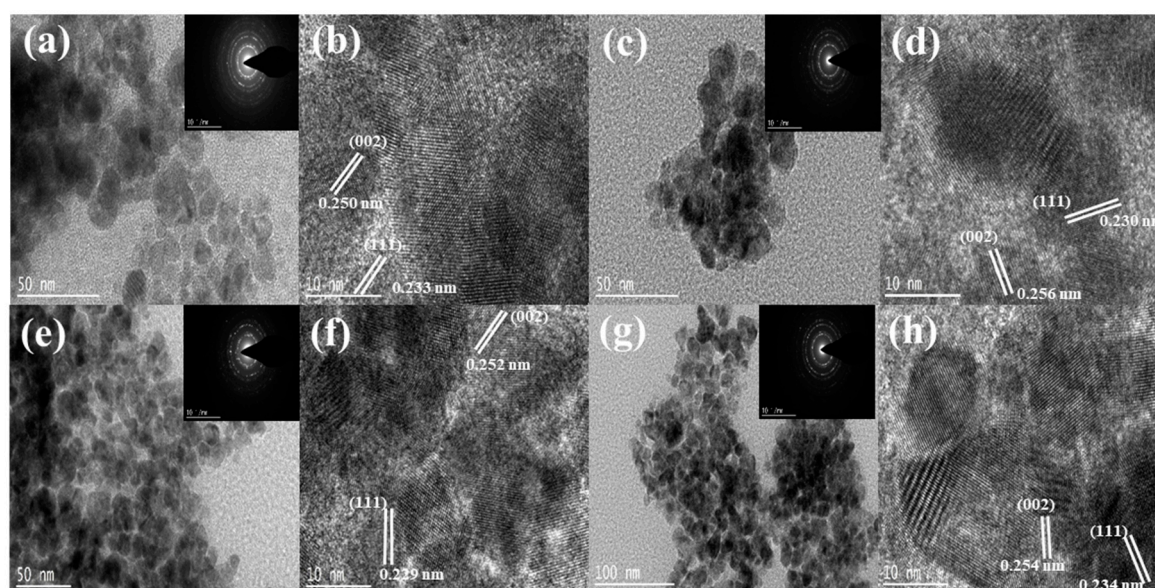


Figure 5. TEM and SAED images of the $15\text{CuO}-z\text{Fe}_2\text{O}_3/\text{M}-\text{Ce}_{80}\text{Zr}_{20}$: (a,b) $15\text{CuO}-1\text{Fe}_2\text{O}_3/\text{M}-\text{Ce}_{80}\text{Zr}_{20}$, (c,d) $15\text{CuO}-3\text{Fe}_2\text{O}_3/\text{M}-\text{Ce}_{80}\text{Zr}_{20}$, (e,f) $15\text{CuO}-5\text{Fe}_2\text{O}_3/\text{M}-\text{Ce}_{80}\text{Zr}_{20}$, (g,h) $15\text{CuO}-7\text{Fe}_2\text{O}_3/\text{M}-\text{Ce}_{80}\text{Zr}_{20}$.

2.1.4. H₂-TPR Analysis

The H₂-TPR profiles of M-Ce80Zr20, 15CuO-3MO_x/M-Ce80Zr20 (MO_x = La₂O₃, Fe₂O₃, PrO₂, Sm₂O₃, MnO₂), and 15CuO-zFe₂O₃/M-Ce80Zr20 catalysts are displayed in Figure 6. As can be seen from Figure 6(1), almost all of the 15CuO/M-Ce80Zr20 and 15CuO-3MO_x/M-Ce80Zr20 catalysts showed similar hydrogen consumption profiles in the intensities and shapes. Specifically, there were two groups of peaks in the range of 197–323 °C and 354–472 °C, which could be attributed to the hydrogen consumption caused by the reduction of CuO and MO_x with various interactions with the M-Ce80Zr20 support. It is also worth noting that the reduction peak intensity in the range of 354–472 °C was larger than the shoulder peak in the range of 197–323 °C. The reduction peak in the range of 354–472 °C should be the reduction peak of the CuO species, because its reduction peak is usually centered around 380 °C, according to the pioneer report [33]. In addition, it can be found from the figure that the M-Ce80Zr20 support showed a broad peak at a higher temperature (620 °C), which can be attributed to the reduction of the surface Ce⁴⁺. It has been reported that the reduction temperature of CuO species should be lower than that of the free CuO when supported on fluorite-type oxides [34]. Therefore, the reduction peak in the range of 197–323 °C could be ascribed to the reduction of the CuO species, which had a closely synergistic effect on the M-Ce80Zr20 supports. As a result, the CuO species could be reduced at relatively lower temperature. The M-Ce80Zr20 carriers greatly promoted the reduction of CuO to a certain degree. Additionally, the lower peak temperature of the 15CuO/M-Ce80Zr20 catalysts might be also derived from the reduction of finely dispersed CuO species weakly interacting with the supports, which has commonly been considered to be the active site for CO oxidation with high efficiency [35,36]. However, the ascription of the wide reduction peaks with strong intensity in the high temperature region (354–472 °C) becomes a bit complicated. On the one hand, they might be partially attributed to the reduction of CuO species strongly interacting with the supports. On the other hand, they might also be attributed to the reduction of surface Ce⁴⁺ in the mesoporous Ce-Zr solid solution supports. Compared with the 15CuO/M-Ce80Zr20 reference catalyst, the reduction peaks of 15CuO-3MO_x/M-Ce80Zr20 (MO_x = La₂O₃, Fe₂O₃, PrO₂, Sm₂O₃, MnO₂) catalysts doped with different metal oxides shifted to the higher reduction temperature region. This indicates that the doping of these metal oxides was helpful for enhancing the metal–support interaction. Therefore, the severe thermal agglomeration the CuO active sites had been effectively avoided during the process of the calcination, as reflected in the above XRD analyses of the 15CuO-MO_x/M-Ce80Zr20.

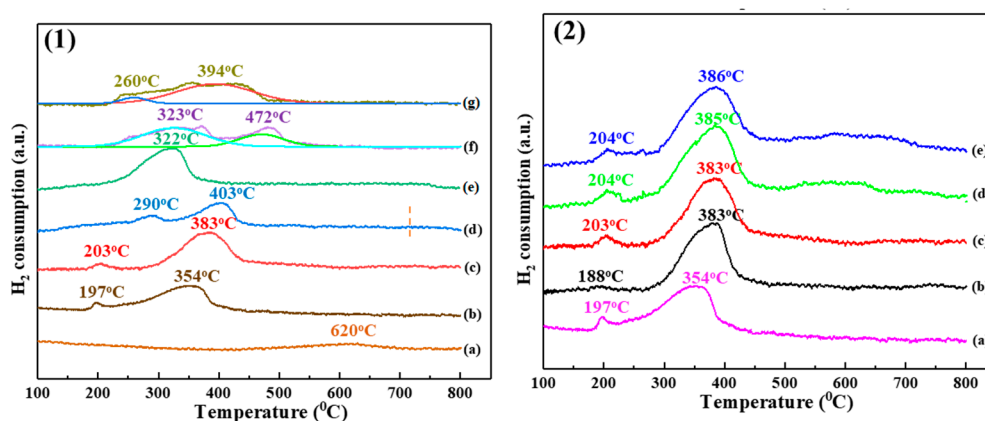


Figure 6. (1) H₂-TPR profiles of M-Ce80Zr20 support and 15CuO-3MO_x/M-Ce80Zr20 (MO_x = La₂O₃, Fe₂O₃, PrO₂, Sm₂O₃, MnO₂) catalysts: (a) M-Ce80Zr20, (b) 15CuO/M-Ce80Zr20, (c) 15CuO-3Fe₂O₃/M-Ce80Zr20, (d) 15CuO-3La₂O₃/M-Ce80Zr20, (e) 15CuO-3MnO₂/M-Ce80Zr20, (f) 15CuO-3Sm₂O₃/M-Ce80Zr20, (g) 15CuO-3PrO₂/M-Ce80Zr20. (2) H₂-TPR profiles of 15CuO-zFe₂O₃/M-Ce80Zr20 catalysts: (a) 15CuO/M-Ce80Zr20, (b) 15CuO-1Fe₂O₃/M-Ce80Zr20, (c) 15CuO-3Fe₂O₃/M-Ce80Zr20, (d) 15CuO-5Fe₂O₃/M-Ce80Zr20, (e) 15CuO-7Fe₂O₃/M-Ce80Zr20.

As for the 15CuO-zFe₂O₃/M-Ce80Zr20 catalysts with different loading amounts of Fe₂O₃, their H₂-TPR profiles were displayed in Figure 6(2). It is noticeable that the 15CuO-zFe₂O₃/M-Ce80Zr20 catalysts display much higher reduction temperatures than the 15CuO/M-Ce80Zr20 reference catalyst. However, with the increase of the Fe₂O₃ loading amount from 1 wt. % to 7 wt. %, both the intensities and positions of the reduction peak suffer no obvious changes. Therefore, the introduction of the Fe₂O₃ dopant could influence the reductivity of the CuO active sites.

2.1.5. XPS Analysis

The surface compositions and chemical states of the elements of the catalysts were analyzed by X-ray photoelectron spectroscopy (XPS) and detailed information related to the surface elements was obtained. The XPS profiles of Cu 2p, Ce 3d, Zr 3d, and O 1s of the 15CuO/M-Ce80Zr20 and 15CuO-3MO_x/M-Ce80Zr20 (MO_x = La₂O₃, Fe₂O₃, PrO₂, Sm₂O₃, MnO₂) catalysts are exhibited in Figure 7, and the corresponding binding energies of these surface elements are summarized in Table 2.

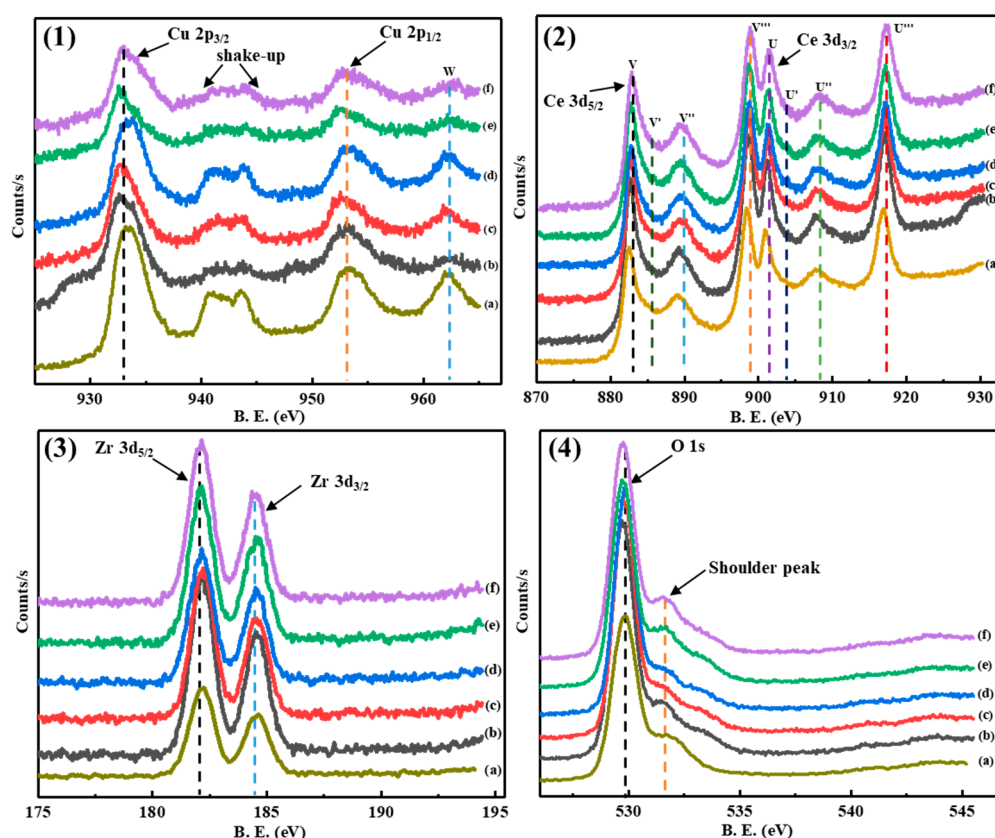


Figure 7. XPS spectra of Cu 2p (1), Ce 3d (2), Zr 3d (3), and O 1s (4) for 15CuO/M-Ce80Zr20 and 15CuO-3MO_x/M-Ce80Zr20 (MO_x = La₂O₃, Fe₂O₃, PrO₂, Sm₂O₃, MnO₂) catalysts: (a) 15CuO/M-Ce80Zr20, (b) 15CuO-3PrO₂/M-Ce80Zr20, (c) 15CuO-3Fe₂O₃/M-Ce80Zr20, (d) 15CuO-3MnO₂/M-Ce80Zr20, (e) 15CuO-3La₂O₃/M-Ce80Zr20, (f) 15CuO-3Sm₂O₃/M-Ce80Zr20.

Table 2. Binding energies (eV) of the surface elements of the catalysts.

Samples	Cu 2p _{3/2}	O 1s	Ce 3d _{5/2}	Zr 3d _{5/2}
15CuO/M-Ce80Zr20	933.3	529.8	882.5	181.3
15CuO-3PrO ₂ /M-Ce80Zr20	933.7	529.5	882.4	181.4
15CuO-3Fe ₂ O ₃ /M-Ce80Zr20	933.1	529.6	882.5	181.5
15CuO-3MnO ₂ /M-Ce80Zr20	933.4	529.8	882.6	181.4
15CuO-3La ₂ O ₃ /M-Ce80Zr20	933.2	529.8	882.7	181.4
15CuO-3Sm ₂ O ₃ /M-Ce80Zr20	933.2	529.8	882.5	181.3

It can be observed in Figure 7(1) that the XPS peaks of Cu 2p are centered at 954.0 eV and 934.0 eV, which could correspond to Cu 2p_{1/2} and Cu 2p_{3/2}, respectively. Avgouropoulos and Ioannides reported that the existence of oscillating peaks in the range of 939.0–944.0 eV and high binding energy of Cu 2p_{3/2} in the range of 933.0 eV–934.0 eV were the two main XPS characteristics of CuO, where the state of copper species is in the Cu²⁺ state [37]. The presence of Cu 2p_{3/2} peak around about 934.0 eV, the shake-up peak in the range of 939.0–944.0 eV, and the satellite W peak around 962.5 eV indicates the presence of CuO species on the surface of 15CuO/M-Ce80Zr20 and 15CuO-3MO_x/M-Ce80Zr20 (MO_x = La₂O₃, Fe₂O₃, PrO₂, Sm₂O₃, MnO₂) catalysts. Additionally, it is worth noting in Table 2 that the introduction of the transitional metal oxides and rare earth metal oxides did not obviously influence the binding energy as well as the coordination environment of Cu²⁺ species.

For the state of the cerium species, it is noticeable in Figure 7(2) that the spectra of Ce 3d can be split into eight peaks centered around 882.0 eV, 885.0 eV, 889.0 eV, 899.0 eV, 901.0 eV, 904.0 eV, 908.0 eV, and 917.0 eV binding energies, which can be categorized into the groups of V and U, according to the pioneer reports [38]. Generally, the peaks categorized into the groups V and U can be attributed to Ce 3d_{5/2} and Ce 3d_{3/2}, respectively. The peaks referred to U''' and V''' can be attributed to the Ce cation in the state of Ce⁴⁺. The U, V, U'' and V'' groups are produced by one or two electrons moving from a filled O 2p orbit to an empty Ce 4f orbit. The presence of U' and V' are due to the presence of Ce³⁺ species [38–41]. The Ce cations in most of the catalysts were mainly present in the form of Ce⁴⁺, and at the same time, the presence of Ce³⁺ was also found. In the case of the present 15CuO/M-Ce80Zr20 and 15CuO-3MO_x/M-Ce80Zr20 catalysts, the U' and V' shoulder peaks can be clearly observed, suggesting the presence of Ce³⁺ species. This would facilitate the activation of oxygen and redox recycling of the catalysts, which would promote the low-temperature catalytic performance toward CO oxidation.

Figure 7(3) shows the Zr 3d XPS spectra of the investigated catalysts. It can be clearly seen in the figure that the binding energy of Zr 3d_{5/2} is around 184.5 eV for almost all the catalysts. This is a typical feature with the presence of Zr⁴⁺ on the surface of these mesoporous catalysts [41,42].

As for the O 1s profiles of the studied catalysts, it can be seen from Figure 7(4) that the profile of each sample exhibits a main peak centered at 530.0 eV and a shoulder peak at around 533.0 eV. It has been reported that the shoulder peak near 533.0 eV should correspond to the O²⁻ species associated with the Ce³⁺, usually generating oxygen pockets or vacancies around them in order to maintain the neutrality of the charge, based on the previous literature [38,43]. Therefore, the shoulder peak of the O 1s at high binding energy was finally formed.

The XPS profiles of La 3d, Sm 3d, Pr 3d, Fe 2p and Mn 2p of the 15CuO-3MO_x/M-Ce80Zr20 (MO_x = La₂O₃, Fe₂O₃, PrO₂, Sm₂O₃, MnO₂) catalysts are shown in Figure 8. As shown in Figure 8(1), the position of the La 3d_{5/2} peak is around 834.0 eV and there is a satellite peak around 838.0 eV. The ΔE between them is at about 4 eV, which is probably the characteristic peak of La³⁺ in La₂(CO₃)₃. When catalyst 15CuO-3La₂O₃/M-Ce80Zr20 was exposed to the atmosphere, its surface La₂O₃ interacted with CO₂ to form La₂(CO₃)₃ [44]. As can be seen for the XPS profile of Sm in Figure 8(2), it can be observed that the peaks of Sm 3d_{3/2} and Sm 3d_{5/2} were centered on 1110.0 eV and 1083.0 eV, respectively. Therefore, Sm was mainly present in the form of Sm³⁺ in catalyst 15CuO-3Sm₂O₃/M-Ce80Zr20 [45]. As for the profile of the Pr 3d_{5/2} in Figure 8(3), its profile overlapped a bit with that of the Ce species. However, compared with 15CuO/M-Ce80Zr20 catalyst without Pr modification, it was noticeable that the Pr 3d_{5/2} XPS profile of catalyst 15CuO-3PrO₂/M-Ce80Zr20 showed an additional peak around 930.0 eV, which was assumed to be the peak of Pr 3d_{5/2} [45,46]. The XPS profiles of Fe 2p of the 15CuO-3Fe₂O₃/M-Ce80Zr20 are shown in Figure 8(4). There are two major peaks Fe 2p_{3/2} and Fe 2p_{1/2} located at around 710.4 eV and 724.3 eV. In addition, a satellite peak was observed at about 718.3 eV. This indicates that Fe was present in the form of Fe³⁺ over the surface of 15CuO-3Fe₂O₃/M-Ce80Zr20 [47,48]. Figure 8(5) shows the Mn 2p XPS spectrum over 15CuO-3MnO₂/M-Ce80Zr20 with Mn 2p_{3/2} peak range at 642.0 eV and of the Mn 2p_{1/2} range at 652.7 eV. This indicates that the Mn species in the 15CuO-3MnO₂/M-Ce80Zr20 catalyst are in the form of Mn⁴⁺ [49–51].

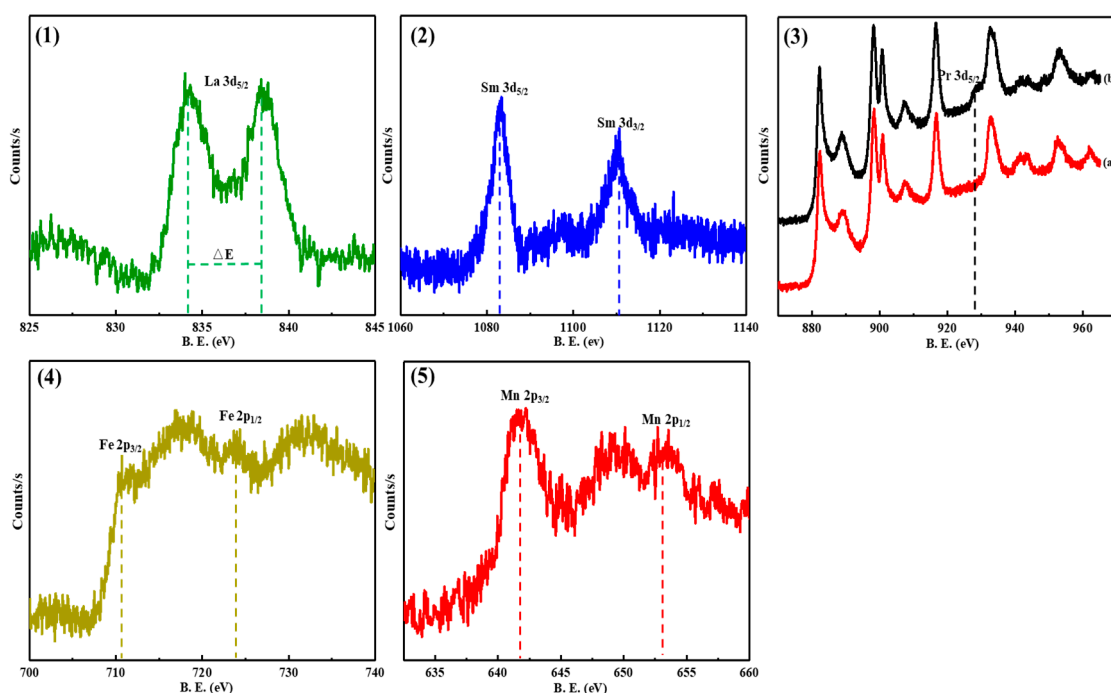


Figure 8. XPS profiles of La 3d (1), Sm 3d (2), Pr 3d (3), Fe 2p (4) and Mn 2p (5) over the 15CuO-3MO_x/M-Ce80Zr20 (MO_x = La₂O₃, Fe₂O₃, PrO₂, Sm₂O₃, MnO₂) catalysts.

2.2. Catalytic Performance toward CO Oxidation

2.2.1. The Evaluation of the Catalytic Activity during the Process of Screening Catalysts

The catalytic activities toward CO oxidation were carried out over the M-Ce80Zr20 support, 15CuO-3MO_x/M-Ce80Zr20 and 15CuO-zFe₂O₃/M-Ce80Zr20 catalysts and their catalytic results are summarized in Figures 9 and 10. The effects of both the types of the metal oxides and the loading amounts of the dopants on the catalytic activities toward CO oxidation were carefully evaluated during the process of screening high-efficiency catalysts.

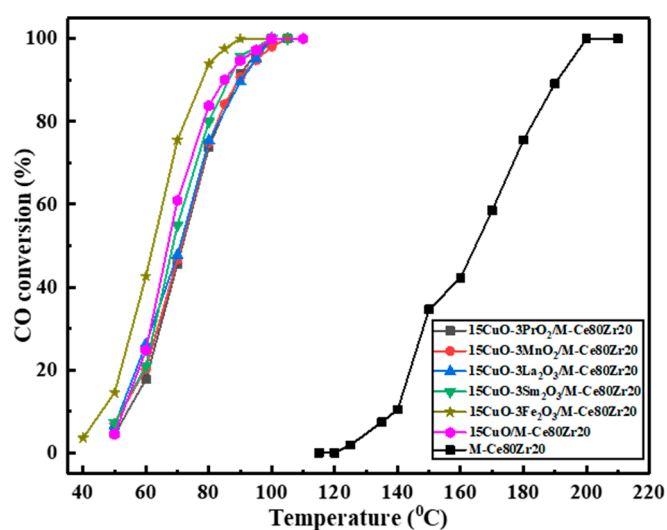


Figure 9. The CO conversion versus reaction temperature over M-Ce80Zr20 support and 15CuO-3MO_x/M-Ce80Zr20 (MO_x = La₂O₃, Fe₂O₃, PrO₂, Sm₂O₃, MnO₂) catalysts; reaction conditions: 1%CO-20%O₂-N₂ balance, GHSV = 12000 mL/(g·h), 1 atm.

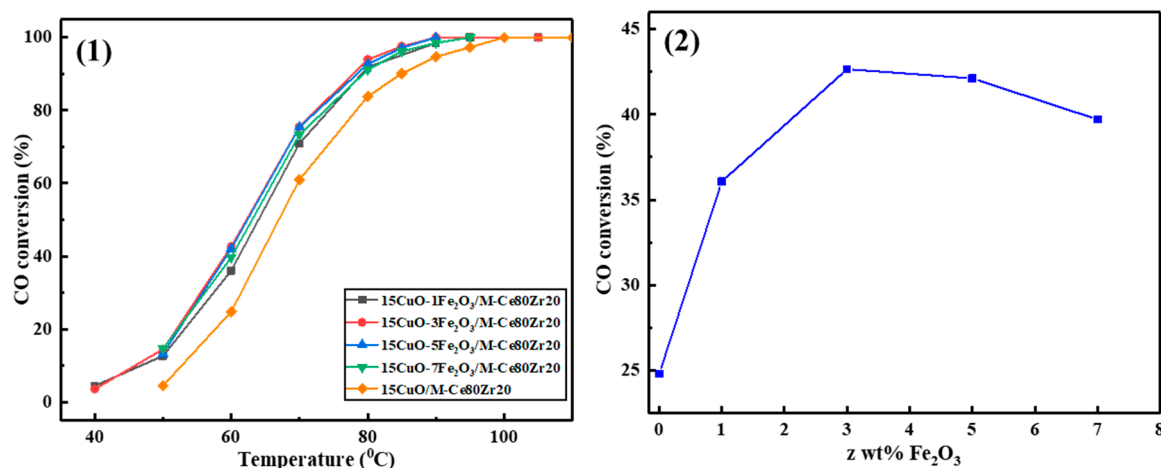


Figure 10. The CO conversion versus reaction temperature over (1) 15CuO-*z*Fe₂O₃/M-Ce80Zr20 catalysts with different Fe₂O₃ loading amounts, (2) the CO conversion versus the loading amounts of Fe₂O₃ (*z*%) over 15CuO-*z*Fe₂O₃/M-Ce80Zr20 catalysts; reaction conditions: 1%CO-20%O₂-N₂ balance, GHSV = 12000 mL/(g·h), 1 atm.

It can be observed in Figure 9 that the catalytic activities of CuO-based mesoporous catalysts (15CuO/M-Ce80Zr20 and 15CuO-3MO_x/M-Ce80Zr20) were significantly higher than that of the corresponding M-Ce80Zr20 catalytic supports, demonstrating the critical role of CuO active site in catalyzing the CO oxidation. Additionally, it is noticeable that the CO conversion gradually increases with the increase in reaction temperature until reaching 100%, which can be attributed to the dynamic control feature of CO oxidation at low temperature. In addition, the 15CuO-3MO_x/M-Ce80Zr20 catalysts also display different catalytic activities from the pristine 15CuO/M-Ce80Zr20 catalyst, although they had identical CuO loading amounts. Among these catalysts, the Fe₂O₃-doped 15CuO-3Fe₂O₃/M-Ce80Zr20 catalyst exhibited much higher catalytic activity than the corresponding counterparts with other dopants (La₂O₃, PrO₂, Sm₂O₃, MnO₂), demonstrating the superiority of Fe₂O₃ as the catalytic modifier. The reason for this can be attributed to the synergistic effect between CuO and Fe₂O₃, which has a strong influence on the catalytic activity of CO low-temperature oxidation. Typically, Fe₂O₃ promotes the reduction of CuO, according to the pioneer report [52]. As a result, the activity of the Fe₂O₃-doped CuO-based catalysts is higher than that of the reference catalyst without modification. Due to the dual function of Fe₂O₃, it can carry out the CO oxidation reaction in the presence and absence of oxygen by losing its lattice oxygen [53]. Therefore, Fe₂O₃ was considered the most promising catalytic promoter toward the CO low-temperature catalytic oxidation process.

The effect of the Fe₂O₃ loading amount on the catalytic activities over 15CuO-*z*Fe₂O₃/M-Ce80Zr20 catalysts is reflected in Figure 10. As can be seen from Figure 10(1), the loading amounts of the Fe₂O₃ greatly influenced the catalytic CO oxidation activity. To better demonstrate the effect of the Fe₂O₃ modification, the CO conversion versus Fe₂O₃ loading amount over 15CuO-*z*Fe₂O₃/M-Ce80Zr20 catalysts at 60 °C is displayed in Figure 10(2), which would more obviously reflect the effect of Fe₂O₃ loading amount (*z*) on the catalytic activity. As observed in Figure 10(1) and (2), the catalytic activity of 15CuO-*z*Fe₂O₃/M-Ce80Zr20 catalysts could be gradually enhanced with the increase of Fe₂O₃ content up to 3 wt. %, and the 15CuO-3Fe₂O₃/M-Ce80Zr20 catalyst exhibited the highest catalytic activity, especially in the low reaction temperature region. However, when the Fe₂O₃ was further increased from 3 wt. % to 7 wt. %, the catalytic activity suffered a great decrease. The reason for this phenomenon might be derived from the poor dispersion of the high loading amounts of Fe₂O₃. The 15CuO-3Fe₂O₃/M-Ce80Zr20 catalyst, which had a high surface area of 43.8 m²/g, exhibited the highest catalytic activity. The high specific surface area of the nanostructured catalyst led to more unsaturated surface coordination sites exposed to the reaction gas, which improved the activity of the catalyst. High specific surface area and narrow mesoporous size distribution could promote the high

dispersion of metal or oxide catalyst nanoparticles, which had a certain beneficial effect on catalytic performance [52].

2.2.2. Long-Term Stability Test

Catalytic stability was also an important concern for CuO-based catalysts toward CO oxidation. Therefore, the long-term stability test of the 15CuO-3Fe₂O₃/M-Ce80Zr20 catalyst was investigated under specific reaction conditions (CO/O₂ = 0.05, GHSV = 12000 mL/(g·h), 70 °C, 1 atm), and the 15CuO-3Fe₂O₃/M-Ce80Zr20 was selected as a representative of the catalyst. It can be observed in Figure 11 that the 15CuO-3Fe₂O₃/M-Ce80Zr20 catalyst not only exhibited high catalytic activity, but also exhibited superior catalytic stability during the entire 50 h stability test. There was no obvious deactivation during the whole 50 h reaction time on stream, demonstrating excellent catalytic stability.

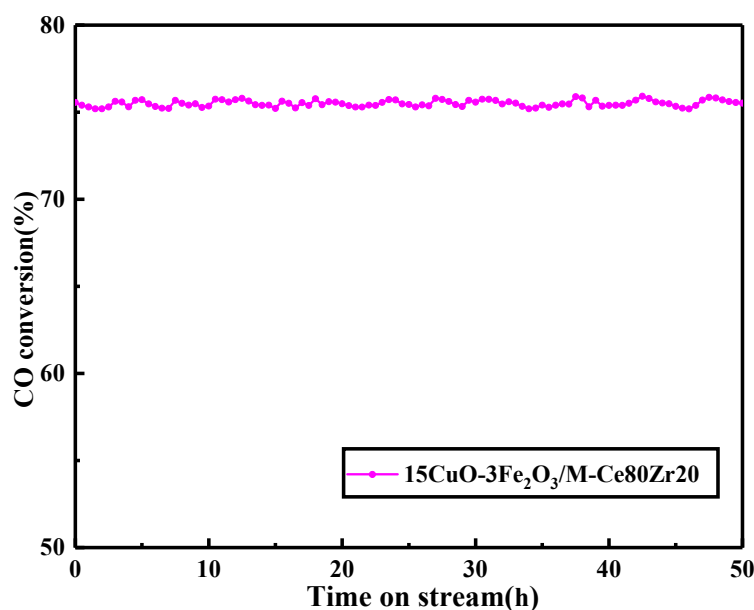


Figure 11. Long-term stability test over the 15CuO-3Fe₂O₃/M-Ce80Zr20 catalyst; reaction conditions: 1%CO-20%O₂-N₂ balance, GHSV = 12000 mL/(g·h), 70 °C, 1 atm.

3. Experimental

3.1. Catalyst Preparation

The mesoporous Ce_{0.8}Zr_{0.2}O₂ solid solution was synthesized by the evaporation-induced self-assembly (EISA) strategy [30]. In a specific synthesis process, 1.0 g of P123 (M_{av} = 5800, EO₂₀PO₇₀EO₂₀, Aladdin) was dissolved in 20.0 mL anhydrous ethanol (C₂H₅OH, Sinopharm Chemical Reagent Co., Ltd., China) and stirred vigorously at room temperature to dissolve. 8 mmol Ce(NO₃)₃·6H₂O (Shanghai Macklin Bio-Chem Co., Ltd., China) and 2 mmol ZrOCl₂·8H₂O (Shanghai Aladdin Bio-Chem Co., Ltd., China) were added to the ethanol solution with a 4:1 molar ratio and stirred at room temperature for at least 4 hours until the solution became transparent. The transparent homogeneous sol was transferred to a Petri dish, which was covered with a PE film with small holes. The petri dish was transferred to an oven with the desired temperature and humidity (temperature: 60 °C, relative humidity: ≤ 50%) for solvent evaporation and template assembly for more than 48 hours. A yellow xerogel was obtained after the EISA process, which was further calcined at 500 °C with a ramping rate of 1 °C/min. The obtained mesoporous material was designated as M-Ce80Zr20.

The Cu(NO₃)₂·6H₂O, La(NO₃)₃·6H₂O, Sm(NO₃)₃·6H₂O, Pr(NO₃)₃·6H₂O, Fe(NO₃)₃·9H₂O, Mn(NO₃)₂·4H₂O (Shanghai Aladdin Bio-Chem Co., Ltd., China) were employed as the precursors of metal oxides. The metal oxide-modified CuO-based with M-Ce80Zr20 support was prepared by an incipient impregnation method, in which the weight percentage of CuO and MO_x (La₂O₃, Fe₂O₃,

PrO₂, Sm₂O₃, and MnO₂) were controlled at 15 wt. % and 3 wt. %, respectively, which were calculated by the following formulas: CuO wt. % = $m_{\text{CuO}} / (m_{\text{CuO}} + m_{\text{MO}_x} + m_{\text{support}}) \times 100\%$; MO_x wt. % = $m_{\text{MO}_x} / (m_{\text{CuO}} + m_{\text{MO}_x} + m_{\text{support}}) \times 100\%$. After impregnation, the catalyst precursor was dried in a 60 °C oven for 24 hours and then calcined at 600 °C for 5 h with a ramping rate of 1 °C/min. The obtained catalyst with 15 wt. % CuO and 3 wt. % MO_x loading was designated as 15CuO-3MO_x/M-Ce80Zr20 (MO_x = La₂O₃, Fe₂O₃, PrO₂, Sm₂O₃, MnO₂). The catalyst with 15 wt. % CuO and z % Fe₂O₃ loading amount was defined as 15CuO-zFe₂O₃/M-Ce80Zr20.

3.2. Catalyst Characterizations

X-ray powder diffraction (XRD) patterns were collected on a XRD-6100 diffractometer (Shimadzu, Japan) using Cu K α radiation at 40 kV and 100 mA in the range of 20°–80° (2 θ) with a step length of 0.02° at a scanning rate of 3°/min.

N₂ physisorption analysis were collected using an Autosorb-iQ-AG-MP instrument (Quantachrome, US) at –196 °C. Before the measurement, samples were degassed at 300 °C for at least 3 h. The specific surface areas of the catalysts were calculated by the multipoint Brunauer–Emmet–Teller (BET) method. The pore size distributions and pore volumes were calculated from the adsorption branches of the isotherms by using the Barrett–Joyner–Halenda (BJH) method.

Transmission electron microscopy (TEM) images, scanning transmission electron microscopy (STEM) images, selected area electron diffraction (SAED), and energy-dispersed spectroscopy (EDS) mapping measurements were carried out on a high-resolution transmission electron microscopy (FEI TECNAI G2 F20) with accelerating voltage of 200 kV. For the sample preparation, they were firstly dispersed in absolute ethanol together with 30 min ultrasonic and then deposited on a carbon-coated copper grid.

X-ray photoelectron spectroscopy (XPS) measurements were performed on an Escalab 250Xi (Thermo Fisher Scientific, US) spectrometer. The powder of the sample was spread and coated on the conductive tape on the sample holder. The binding energies were calibrated using the C 1s line at 284.5 eV as the reference.

H₂ temperature programmed reduction (H₂-TPR) experiments were performed on homemade fixed bed reactor and the consumption of H₂ was recorded by a LC-D200 mass spectrometer (TILON, US) by using 200 mg catalyst under the mixture of 5 vol % H₂-95 vol % Ar stream (50 mL/min). Prior to the H₂-TPR measurements, the samples were purged with the Ar stream at 300 °C for 30 min and cooled down to room temperature. Then, 5 vol % H₂-95 vol % Ar mixture was introduced, and the programmed temperature was conducted with a ramping heating rate of 20 °C/min to 800 °C. The hydrogen consumption was measured using a LC-D200 mass spectrometer.

3.3. Catalytic Activity Evaluation

Catalytic activity tests for CO oxidation were carried out in a vertical fixed-bed continuous flow quartz reactor. The entire reaction and analysis system consists of three parts: (1) the mass flow controlling unit (Brooks Instruments), (2) the reactor unit (homemade furnace), and (3) the analysis unit (PerkinElmer Gas Chromatography Clarus 680). Typically, 100 mg of catalyst was placed over the quartz wool in the quartz tube of the fixed-bed reactor. The feed gas consisting of 1 vol % CO, 20 vol % O₂ and balanced N₂ with a total flow rate of 20 mL/min, corresponding to the gas hourly space velocity (GHSV) of 12000 mL/(g·h) gas, was introduced into the reactor and investigated with designated temperature range. Finally, the effluent gas was analyzed online using the GC-680 Perkin Elmer gas chromatography equipped with a thermal conductivity detector (TCD). The catalytic activity was reflected and expressed in the form of CO conversion. Therefore, the CO conversion (abbreviated as C_{CO}) can be calculated based on the carbon balance according to the following formula, where the F_{CO, inlet} and F_{CO, outlet} represented the flow rate of CO species into and out of the reactor.

$$C_{\text{CO}} = (F_{\text{CO, inlet}} - F_{\text{CO, outlet}}) / F_{\text{CO, inlet}} \times 100\% \quad (1)$$

4. Conclusions

A series of metal oxide (La_2O_3 , Fe_2O_3 , PrO_2 , Sm_2O_3 , and MnO_2)-doped CuO-based catalysts supported on mesoporous $\text{Ce}_{0.8}\text{Zr}_{0.2}\text{O}_2$ were prepared by incipient impregnation method and used directly as catalysts for CO catalytic oxidation. This study demonstrated that doped transition metal oxides could regulate the oxygen mobility and reduction ability of catalysts and the high dispersion of rare earth metal oxides (PrO_2 , Sm_2O_3) could prevent the thermal sintering and aggregation of CuO-based catalysts during the process of calcination. It was found that the CuO-based catalysts with 3 wt. % Fe_2O_3 loading amount exhibited the highest catalytic activity. Compared with other catalysts, the 15CuO-3Fe₂O₃/M-Ce80Zr20 catalyst exhibited much higher catalytic activity at low temperature. This was due to the synergistic effect between CuO and Fe_2O_3 and the dual function of Fe_2O_3 by losing its lattice oxygen. Moreover, these mesoporous catalysts had no deactivation phenomenon after 50 h stability test, demonstrating outstanding catalytic stability. In conclusion, the present Fe_2O_3 doped CuO-based catalysts supported on mesoporous $\text{Ce}_{0.8}\text{Zr}_{0.2}\text{O}_2$ solid solution can be used as a series of promising catalysts with intensified low-temperature activity toward CO oxidation.

Author Contributions: Conceptualization, Y.C. and L.X.; methodology, Y.C., L.X., M.C. and X.H.; software, Y.C., C.L. and X.L.; validation, C.W., B.Y., Z.M. and F.W.; formal analysis, Y.C. and L.X.; investigation, M.C.; resources, M.C.; data curation, C.W., B.Y., Z.M. and F.W.; writing—original draft preparation, Y.C.; writing—review and editing, Y.C. and L.X.; visualization, L.X., M.C. and X.H.; supervision, L.X., M.C., Z.M. and X.H.; project administration, M.C.; funding acquisition, M.C.

Funding: The authors sincerely acknowledge the financial support from National Natural Science Foundation of China (Grant No. 21503113, 21577065, 21503142, and 91543115), National Key Research and Development Program of China (2018YFC0213802), International ST Cooperation Program of China (2014DFA90780), Environmental Protection Projects of Jiangsu province (2017022) and a Project Funded by the Priority Academic Program Development of Jiangsu Higher Education Institutions. This study is also supported by Startup Foundation of Nanjing University of Information Science & Technology.

Conflicts of Interest: There are no conflict to declare.

References

1. Topacoglu, H.; Katsakoglou, S.; Ipekci, A. Effect of exhaust emissions on carbon monoxide levels in employees working at indoor car wash facilities. *Hippokratia* **2014**, *18*, 37. [[PubMed](#)]
2. Hampson, N.B.; Holm, J.R. Suicidal carbon monoxide poisoning has decreased with controls on automobile emissions. *Undersea Hyperb. Med.* **2015**, *42*, 159–164. [[PubMed](#)]
3. Green, I.X.; Tang, W.; Neurock, M.; Yates, J.T. Spectroscopic observation of dual catalytic sites during oxidation of CO on a Au/TiO₂ catalyst. *Science* **2011**, *333*, 736–739. [[CrossRef](#)] [[PubMed](#)]
4. Zhang, W.; Cheng, D.; Zhu, J. Theoretical study of CO catalytic oxidation on free and defective graphene-supported Au–Pd bimetallic clusters. *RSC Adv.* **2014**, *4*, 42554–42561. [[CrossRef](#)]
5. Zou, Z.Q.; Meng, M.; Zha, Y.Q. Surfactant-Assisted Synthesis, Characterizations, and Catalytic Oxidation Mechanisms of the Mesoporous MnO_x–CeO₂ and Pd/MnO_x–CeO₂ Catalysts Used for CO and C₃H₈ Oxidation. *J. Phys. Chem. C* **2014**, *114*, 468–477. [[CrossRef](#)]
6. Haruta, M.; Yamada, N.; Kobayashi, T.; Iijima, S. Gold catalysts prepared by coprecipitation for low-temperature oxidation of hydrogen and of carbon monoxide. *J. Catal.* **1989**, *115*, 301–309. [[CrossRef](#)]
7. Wang, C.; Cheng, Q.; Wang, X.; Ma, K.; Bai, X.; Tan, S.; Ye, T.; Tong, D.; Zheng, L.; Jing, Z.; et al. Enhanced catalytic performance for CO preferential oxidation over CuO catalysts supported on highly defective CeO₂ nanocrystals. *Appl. Surf. Sci.* **2017**, *422*, 932–943. [[CrossRef](#)]
8. Guo, X.; Li, J.; Zhou, R. Catalytic performance of manganese doped CuO–CeO₂ catalysts for selective oxidation of CO in hydrogen-rich gas. *Fuel* **2016**, *163*, 56–64. [[CrossRef](#)]
9. Liu, S.; Wei, Z.; Deng, T.; Dong, W.; Zheng, W. Mechanistic Origin of Enhanced CO Catalytic Oxidation over Co₃O₄/LaCoO₃ at Lower Temperature. *Chemcatchem* **2017**, *9*, 3102–3106. [[CrossRef](#)]
10. Hu, L.; Sun, K.; Peng, Q.; Xu, B.; Li, Y. Surface active sites on Co₃O₄ nanobelt and nanocube model catalysts for CO oxidation. *Nano Res.* **2010**, *3*, 363–368. [[CrossRef](#)]
11. Gamboa-Rosales, N.K.; Ayastuy, J.L.; Boukha, Z.; Bion, N.; Duprez, D.; Pérez-Omil, J.A.; del Rio, E.; Gutierrez-Ortiz, M.A. Ceria-supported Au–CuO and Au–Co₃O₄ catalysts for CO oxidation: An 18O/16O isotopic exchange study. *Appl. Catal. B Environ.* **2015**, *168*, 87–97. [[CrossRef](#)]

12. Chen, G.; Xu, Q.; Yang, Y.; Li, C.; Huang, T.; Sun, G.; Zhang, S.; Ma, D.; Li, X. Facile and mild strategy to construct mesoporous CeO₂-CuO nanorods with enhanced catalytic activity toward CO oxidation. *ACS Appl. Mater. Interfaces* **2015**, *7*, 23538–23544. [[CrossRef](#)] [[PubMed](#)]
13. Laguna, O.H.; Pérez, A.; Centeno, M.A.; Odriozola, J.A. Synergy between gold and oxygen vacancies in gold supported on Zr-doped ceria catalysts for the CO oxidation. *Appl. Catal. B Environ.* **2015**, *176*, 385–395. [[CrossRef](#)]
14. Min, K.; Min, W.S.; Chang, H.L. Catalytic carbon monoxide oxidation over CoO_x/CeO₂ composite catalysts. *Appl. Catal. A Gen.* **2003**, *251*, 143–156.
15. Moretti, E.; Storaro, L.; Talon, A.; Lenarda, M.; Riello, P.; Frattini, R.; Mdm, D.Y.; Jimenez-Lopez, A.; Rodriguez-Castellon, E.; Ternero, F.; et al. Effect of thermal treatments on the catalytic behaviour in the CO preferential oxidation of a CuO-CeO₂-ZrO₂ catalyst with a flower-like morphology. *Appl. Catal. B Environ.* **2011**, *102*, 627–637. [[CrossRef](#)]
16. Narula, C.K.; Haack, L.P.; Chun, W.; Jen, H.W.; Graham, G.W. Single-Phase PrO_y-ZrO₂ Materials and Their Oxygen Storage Capacity: A Comparison with Single-Phase CeO₂-ZrO₂, PrO_y-CeO₂, and PrO_y-CeO₂-ZrO₂ Materials. *Phys. Chem. B* **1999**, *103*, 3634–3639. [[CrossRef](#)]
17. Wang, J.A.; Chen, L.F.; Valenzuela, M.A.; Montoya, A.; Salmones, J.; Del Angel, P. Rietveld refinement and activity of CO oxidation over Pd/Ce_{0.8}Zr_{0.2}O₂ catalyst prepared via a surfactant-assisted route. *Appl. Surf. Sci.* **2004**, *230*, 34–43. [[CrossRef](#)]
18. Si, R.; Zhang, Y.W.; Xiao, C.X.; Li, S.J.; Lin, B.X.; Kou, Y.; Yan, C.H. Non-Template Hydrothermal Route Derived Mesoporous Ce_{0.2}Zr_{0.8}O₂ Nanosized Powders with Blue-Shifted UV Absorption and High CO Conversion Activity. *ChemInform* **2004**, *6*, 1056–1063. [[CrossRef](#)]
19. Wang, S.P.; Zhang, T.Y.; Su, Y.; Wang, S.R.; Zhang, S.M.; Zhu, B.L.; Wu, S.H. An Investigation of Catalytic Activity for CO Oxidation of CuO/Ce_xZr_{1-x}O₂ Catalysts. *Catal. Lett.* **2008**, *121*, 70–76. [[CrossRef](#)]
20. Cui, Y.; Lian, X.; Xu, L.; Chen, M.; Yang, B.; Wu, C.-E.; Li, W.; Huang, B.; Hu, X. Designing and Fabricating Ordered Mesoporous Metal Oxides for CO₂ Catalytic Conversion: A Review and Prospect. *Materials* **2019**, *12*, 276. [[CrossRef](#)]
21. Kikugawa, M.; Yamazaki, K.; Shinjoh, H. Characterization and catalytic activity of CuO/TiO₂-ZrO₂ for low temperature CO oxidation. *Appl. Catal. A Gen.* **2017**, *547*, 199–204. [[CrossRef](#)]
22. Zhong, Z.; Ho, J.; Teo, J.; Shen, S.; Gedanken, A. Synthesis of Porous α-Fe₂O₃ Nanorods and Deposition of Very Small Gold Particles in the Pores for Catalytic Oxidation of CO. *Chem. Mater.* **2007**, *19*, 69–73. [[CrossRef](#)]
23. Fu, Z.D.; Ye, Q.; Cheng, S.Y.; Wang, D. Catalytic Oxidation of CO over Ag-Doped Manganese Oxide Catalysts: Preparation and Catalytic Activity. *Adv. Mater. Res.* **2015**, *1089*, 133–136. [[CrossRef](#)]
24. Dongsheng, Q.I.A.O.; Guanzhong, L.U.; Yun, G.U.O.; Yanqin, W.A.N.G.; Yanglong, G.U.O. Effect of water vapor on the CO and CH₄ catalytic oxidation over CeO₂-MO_x (M= Cu, Mn, Fe, Co, and Ni) mixed oxide. *J. Rare Earths* **2010**, *28*, 742–746.
25. Li, Y.; Zhang, X.; Long, E.; Li, H.; Wu, D.; Cai, L.; Gong, M.; Chen, Y. Influence of CeO₂ and La₂O₃ on properties of palladium catalysts used for emission control of natural gas vehicles. *J. Nat. Gas. Chem.* **2009**, *18*, 415–420. [[CrossRef](#)]
26. Duan, D.; Hao, C.; Shi, W.; Wang, H.; Sun, Z. Sm₂O₃/Co₃O₄ catalysts prepared by dealloying for low-temperature CO oxidation. *RSC Adv.* **2018**, *8*, 11289–11295. [[CrossRef](#)]
27. Wang, J.B.; Shih, W.H.; Huang, T.J. Study of Sm₂O₃-doped CeO₂/Al₂O₃-supported copper catalyst for CO oxidation. *Appl. Catal. A Gen.* **2000**, *203*, 191–199. [[CrossRef](#)]
28. Zhao, Z.J.; Wang, R.Y.; Zhao, Q.L.; Wang, E.P.; Su, H.Q.; Zeng, S.H. CuO/CeO₂ and CuO/PrO₂-CeO₂ Catalysts for Preferential Oxidation of CO. *Adv. Mater. Res.* **2013**, *773*, 601–605. [[CrossRef](#)]
29. Zhang, X.B.; Ma, K.Y.; Zhang, L.H.; Yong, G.P.; Dai, Y.; Liu, S.M. Effect of precipitation method and Ce doping on the catalytic activity of copper manganese oxide catalysts for CO oxidation. *Chinese. J. Chem. Phys.* **2011**, *24*, 97. [[CrossRef](#)]
30. Xu, L.; Lian, X.; Chen, M.; Cui, Y.; Wang, F.; Li, W.; Huang, B. CO₂ methanation over CoNi bimetal-doped ordered mesoporous Al₂O₃ catalysts with enhanced low-temperature activities. *Int. J. Hydrogen. Energ.* **2018**, *43*, 17172–17184. [[CrossRef](#)]
31. Cao, J.L.; Wang, Y.; Zhang, T.Y.; Wu, S.H.; Yuan, Z.Y. Preparation, characterization and catalytic behavior of nanostructured mesoporous CuO/Ce_{0.8}Zr_{0.2}O₂ catalysts for low-temperature CO oxidation. *Appl. Catal. B Environ.* **2008**, *78*, 120–128. [[CrossRef](#)]

32. Sing, K.S.W. Reporting physisorption data for gas/solid systems with special reference to the determination of surface area and porosity (Recommendations 1984). *Pure Appl. Chem.* **1985**, *57*, 603–619. [[CrossRef](#)]
33. Lin, R.; Luo, M.F.; Zhong, Y.J.; Yan, Z.L.; Liu, G.Y.; Liu, W.P. Comparative study of CuO/Ce_{0.7}Sn_{0.3}O₂, CuO/CeO₂ and CuO/SnO₂ catalysts for low-temperature CO oxidation. *Appl. Catal. A Gen.* **2003**, *255*, 331–336.
34. Radlik, M.; Adamowska, M.; Łamacz, A.; Krztoń, A.; Da Costa, P.; Turek, W. Study of the surface evolution of nitrogen species on CuO/CeZrO₂ catalysts. *Reactn. Kinets. Mech. Catal.* **2013**, *109*, 43–56. [[CrossRef](#)]
35. Luo, M.F.; Ma, J.M.; Lu, J.Q.; Song, Y.P.; Wang, Y.J. High-surface area CuO–CeO₂ catalysts prepared by a surfactant-templated method for low-temperature CO oxidation. *J. Catal.* **2007**, *246*, 52–59. [[CrossRef](#)]
36. Luo, M.F.; Zhong, Y.J.; Yuan, X.X.; Zheng, X.M. TPR and TPD studies of CuO/CeO₂ catalysts for low temperature CO oxidation. *Appl. Catal. A Gen.* **1997**, *162*, 121–131. [[CrossRef](#)]
37. Avgouropoulos, G.; Ioannides, T. Selective CO oxidation over CuO–CeO₂ catalysts prepared via the urea–nitrate combustion method. *Appl. Catal. A Gen.* **2003**, *244*, 155–167. [[CrossRef](#)]
38. Sukonket, T.; Khan, A.; Saha, B.; Ibrahim, H.; Tantayanon, S.; Kumar, P.; Idem, R. Influence of the catalyst preparation method, surfactant amount, and steam on CO₂ reforming of CH₄ over 5Ni/Ce_{0.6}Zr_{0.4}O₂ catalysts. *Energ. Fuel.* **2011**, *25*, 864–877. [[CrossRef](#)]
39. Liu, C.J.; Ye, J.; Jiang, J.; Pan, Y. Progresses in the preparation of coke resistant Ni-based catalyst for steam and CO₂ reforming of methane. *Chemcatchem* **2011**, *3*, 529–541. [[CrossRef](#)]
40. Du, X.; Zhang, D.; Shi, L.; Gao, R.; Zhang, J. Morphology dependence of catalytic properties of Ni/CeO₂ nanostructures for carbon dioxide reforming of methane. *J. Phys. Chem. C* **2012**, *116*, 10009–10016. [[CrossRef](#)]
41. Reddy, B.M.; Khan, A.; Yamada, Y.; Kobayashi, T.; Loridant, S.; Volta, J.C. Surface characterization of CeO₂/SiO₂ and V₂O₅/CeO₂/SiO₂ catalysts by Raman, XPS, and other techniques. *J. Phys. Chem. B* **2002**, *106*, 10964–10972. [[CrossRef](#)]
42. Galtayries, A.; Sporcken, R.; Riga, J.; Blanchard, G.; Caudano, R. XPS comparative study of ceria/zirconia mixed oxides: powders and thin film characterisation. *J. Electron. Spectrosc.* **1998**, *88*, 951–956. [[CrossRef](#)]
43. Reddy, B.M.; Khan, A. Nanosized CeO₂–SiO₂, CeO₂–TiO₂, and CeO₂–ZrO₂ mixed oxides: Influence of supporting oxide on thermal stability and oxygen storage properties of ceria. *Catal. Surv. Asia* **2005**, *9*, 155–171. [[CrossRef](#)]
44. Milt, V.G.; Spretz, R.; Ulla, M.A.; Lombardo, E.A.; Fierro, J.G. The nature of active sites for the oxidation of methane on La-based perovskites. *Catal. Lett.* **1996**, *42*, 57–63. [[CrossRef](#)]
45. Uwamino, Y.; Ishizuka, T.; Yamatera, H. X-ray photoelectron spectroscopy of rare-earth compounds. *J. Electron. Spectrosc.* **1984**, *34*, 67–78. [[CrossRef](#)]
46. Sarma, D.D.; Rao, C.N.R. XPS studies of oxides of second-and third-row transition metals including rare earths. *J. Electron. Spectrosc.* **1980**, *20*, 25–45. [[CrossRef](#)]
47. Yadav, R.S.; Havlica, J.; Masilko, J.; Kalina, L.; Wasserbauer, J.; Hajdúchová, M.; Enev, V.; Kuřitka, I.; Kožáková, Z. Impact of Nd³⁺ in CoFe₂O₄ spinel ferrite nanoparticles on cation distribution, structural and magnetic properties. *J. Magn. Magn. Mater.* **2016**, *399*, 109–117. [[CrossRef](#)]
48. Hong, L.Y.; Yong, Q.W.; Shao, M.Z.; Li, S.L.; Xi, L.C.; Shi, Y.L.; Rui, J.Y.; Yao, M.H.; Ning, L. Low-Temperature Preparation of Superparamagnetic CoFe₂O₄ Microspheres with High Saturation Magnetization. *Nanoscale Res. Lett.* **2010**, *5*, 1817–1821.
49. Li, J.; Zhu, P.; Zuo, S.; Huang, Q.; Zhou, R. Influence of Mn doping on the performance of CuO–CeO₂ catalysts for selective oxidation of CO in hydrogen-rich streams. *Appl. Catal. A Gen.* **2010**, *381*, 261–266. [[CrossRef](#)]
50. Rosso, J.J.; Hochella, M.F., Jr. Natural Iron and Manganese Oxide Samples by XPS. *Surf. Sci. Spectra* **1996**, *4*, 253–265. [[CrossRef](#)]
51. Stranick, M.A. Mn₂O₃ by XPS. *Surf. Sci. Spectra* **1999**, *6*, 39–46. [[CrossRef](#)]
52. Cao, J.L.; Wang, Y.; Yu, X.L.; Wang, S.R.; Wu, S.H.; Yuan, Z.Y. Mesoporous CuO–Fe₂O₃ composite catalysts for low-temperature carbon monoxide oxidation. *Appl. Catal. B Environ.* **2008**, *79*, 26–34. [[CrossRef](#)]
53. Said, A.E.A.A.; El-Wahab, M.M.A.; Goda, M.N. Synthesis and characterization of pure and (Ce, Zr, Ag) doped mesoporous CuO–Fe₂O₃ as highly efficient and stable nanocatalysts for CO oxidation at low temperature. *Appl. Surf. Sci.* **2016**, *390*, 649–665. [[CrossRef](#)]

